Regional variation of microtubule flux reveals microtubule organization in the metaphase meiotic spindle

Ge Yang,[1] Lisa A. Cameron,[2] Paul S. Maddox,[2] Edward D. Salmon,[2] and Gaudenz Danuser[1]

[1]Department of Cell Biology, Scripps Research Institute, La Jolla, CA 92037
[2]Department of Biology, University of North Carolina at Chapel Hill, Chapel Hill, NC 27599

Continuous poleward movement of tubulin is a hallmark of metaphase spindle dynamics in higher eukaryotic cells and is essential for stable spindle architecture and reliable chromosome segregation. We use quantitative fluorescent speckle microscopy to map with high resolution the spatial organization of microtubule flux in *Xenopus laevis* egg extract meiotic spindles. We find that the flux velocity decreases near spindle poles by ~20%. The regional variation is independent of functional kinetochores and centrosomes and is suppressed by inhibition of dynein/dynactin, kinesin-5, or both. Statistical analysis reveals that tubulin flows in two distinct velocity modes. We propose an association of these modes with two architecturally distinct yet spatially overlapping and dynamically cross-linked arrays of microtubules: focused polar microtubule arrays of a uniform polarity and slower flux velocities are interconnected by a dense barrel-like microtubule array of antiparallel polarities and faster flux velocities.

Introduction

In higher eukaryotes, metaphase spindles establish steady-state poleward flux of tubulin subunits (Mitchison, 1989; 2005; Rogers et al., 2005; Kwok and Kapoor, 2007). Proposed flux-driving mechanisms include "reeling in" and disassembly of microtubules at the poles and motor-based sliding of overlapping antiparallel microtubules. The reeling-in mechanism is supported by evidence from *Drosophila melanogaster* embryos (Rogers et al., 2004), human U2OS cells (Ganem and Compton, 2004; Ganem et al., 2005), and vertebrate PtK1 cells (Cameron et al., 2006). However, inhibition of microtubule disassembly had only a minor effect on flux in *Xenopus laevis* egg extract meiotic spindles (Ohi et al., 2007). Instead, tetrameric kinesin-5 has been identified to push apart overlapping antiparallel microtubules (Miyamoto et al., 2004; Shirasu-Hiza et al., 2004; Kapitein et al., 2005). In this mechanism, steady-state spindle length may be maintained either by matching the rates of microtubule sliding and minus end depolymerization at the poles or by coupling sliding with microtubule nucleation and plus end disassembly throughout the spindle (Burbank et al., 2007; Ohi et al., 2007). Other driving mechanisms involving, for example, microtubule plus end–tracking proteins, plus end–directed molecular motors, chromokinesins, or microtubule-severing enzymes may also exist (Maiato et al., 2005; Buster et al., 2007; Kwok and Kapoor, 2007; Zhang et al., 2007).

However, it is not clear whether multiple mechanisms coexist and how they may cooperate to organize microtubules into the compact spindle architecture. Addressing these questions has been challenging because changes in one mechanism will likely lead to compensatory changes in other mechanisms. Thus, flux changes observed under molecular perturbation of specific spindle components are difficult to interpret in terms of the contributions of individual mechanisms.

In this study, we tested whether poleward flux exhibits spatial-temporal patterns that would support the coexistence of distinct mechanisms. The *Xenopus* extract spindles are particularly suitable for this approach, as they are amenable to high resolution

G. Yang and L.A. Cameron contributed equally to this paper.

Correspondence to Edward D. Salmon: tsalmon@email.unc.edu; or Gaudenz Danuser: gdanuser@scripps.edu

P.S. Maddox's present address is Dept. of Pathology and Cell Biology, University of Montreal, Montreal QC H3C 3J7, Canada.

Abbreviations used in this paper: BIC, Bayesian information criterion; FSM, fluorescent speckle microscopy.

The online version of this article contains supplemental material.

The Rockefeller University Press $30.00
J. Cell Biol. Vol. 182 No. 4 631–639
www.jcb.org/cgi/doi/10.1083/jcb.200801105

fluorescent speckle microscopy (FSM) and sensitive statistical analysis of flux variation at the level of individual tubulin subunits. Using this approach, we found two and only two classes of speckles with distinct flux behavior, which were also distinguishable in spindles lacking functional kinetochores and centrosomes but merged into a single class when kinesin-5, dynein/dynactin, or both were inhibited. Together, these results suggest a model for the meiotic spindle in which two focused polar arrays of microtubules with uniform polarity and slower flux rates are interconnected by a dense barrel-like array of microtubules with antiparallel polarity and faster flux rates.

Results and discussion

During metaphase, meiotic spindles formed in *Xenopus* egg extract (Fig. 1 A and Video 1, available at http://www.jcb.org/cgi/content/full/jcb.200801105/DC1) enter a steady state of microtubule turnover in which tubulin subunits are incorporated at microtubule plus ends and are transported poleward, as observed by photoactivation (Mitchison, 1989) and FSM (Waterman-Storer et al., 1998; Maddox et al., 2003a). Although FSM time-lapse videos display in great detail the flux behavior across the spindle, previous FSM studies of extract spindles could not take advantage of this information because of limitations in the image analysis: kymograph analysis (Maddox et al., 2003a) and cross-correlation tracking of the speckle pattern (Miyamoto et al., 2004) yielded only average flux rates in selected regions of the spindle, and initial attempts to track individual speckles were restricted to mapping the density of speckles moving in opposite directions (Vallotton et al., 2003).

In this study, we mapped microtubule flux at the single-speckle level with the goal of investigating flux heterogeneity as an indicator of distinct flux-driving mechanisms. We modified existing particle-tracking methods to retrieve the trajectories of individual speckles in interlaced flux fields with antiparallel directions (Fig. 1, B and C; and Video 1; Yang et al., 2005; Cameron et al., 2006). Typically, we acquired several thousand speckle trajectories per spindle (see FSM image analysis section; Fig. 1, D and E). In control spindles, the average speckle velocity was 2.56 µm/min (n = 66,711 trajectories from 11 spindles), which is consistent with previous studies (Maddox et al., 2003a; Vallotton et al., 2003; Gaetz and Kapoor, 2004; Miyamoto et al., 2004). However, in contrast to Miyamoto et al. (2004), we found that the variation in the mean speckle velocities between spindles was much smaller (~0.11 µm/min; n = 11 spindles) than the variation of individual speckle velocities within a single spindle (SD = 0.61 µm/min; Fig. S1, available at http://www.jcb.org/cgi/content/full/jcb.200801105/DC1). Thus, speckle velocities pooled from multiple spindles reflect the flux variation of tubulin subunits within one spindle.

Maps of speckle trajectories revealed decreased flux rates near the poles (Fig. 1 D), which is in qualitative agreement with findings in Burbank et al. (2007). To further quantify this regional trend, we defined 23 bands of uniform width along the pole-to-pole axis (Fig. 1 F) and analyzed speckle velocities within each band (Fig. 1 G). Average flux rates remained constant over approximately two thirds of the spindle from the spindle midzone but then decreased near the spindle poles by ~20% (Fig. 1 H). Flux rates in regions 1–2 and 22–23 were significantly different from those in regions 11–13 ($P < 0.001$ using a two-sample two-sided t test). However, the trajectories of individual speckles showed neither a decrease in flux by ~100% nor directional reversals at the poles, two key predictions of the slide and cluster model in Burbank et al. (2007). In contrast, our data suggest that tubulin flux is balanced by microtubule depolymerization at the poles.

We considered several factors that could explain slower flux at the poles. First, we excluded the possibility of an imaging

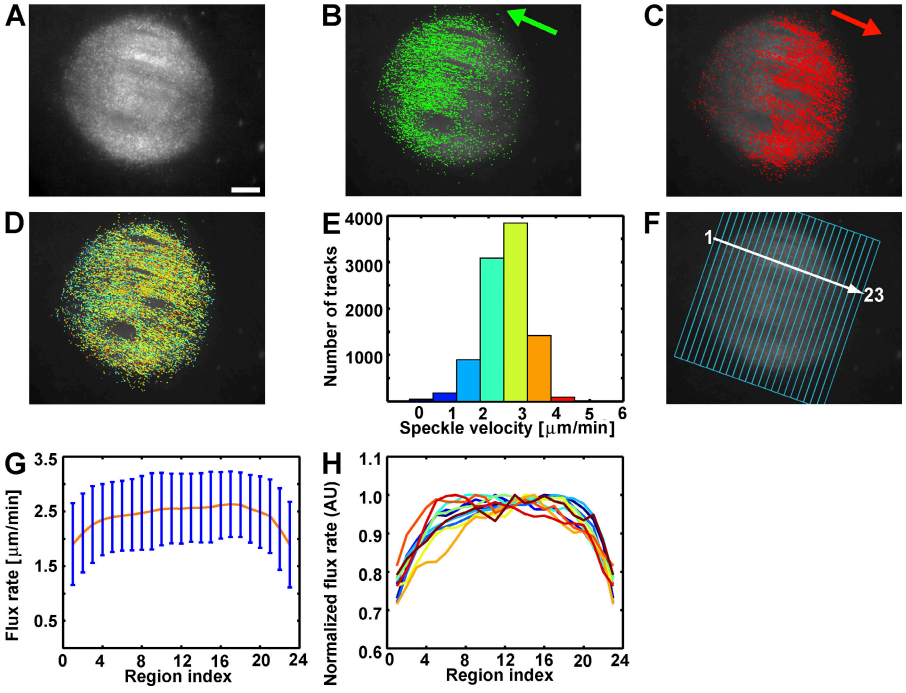

Figure 1. **Regional variation of poleward microtubule flux in control *Xenopus* egg extract spindles.** (A) X-rhodamine tubulin speckles. (B and C) Speckle trajectories separated by direction of poleward movement. Green and red arrows indicate flux towards the left and right poles, respectively. (D and E) Speckle trajectories color coded according to the velocity histogram (E); the flux rate of the spindle shown is mean ± SD = 2.52 ± 0.65 µm/min (n = 9,562 trajectories). (F) Definition of 23 regions along the pole-to-pole axis. (G) Mean and SD (error bars) of speckle velocities within regions in F. (H) Spatial distributions of normalized speckle velocities of 11 control spindles. Bar, 10 µm.

artifact caused by microtubule bending at the poles (see section Excluding spindle geometry as the source of flux…). Then, we analyzed microtubule flux in spindles assembled around plasmid DNA-coated magnetic beads, which lack both functional kinetochores and centrosomes (Fig. 2 A and Video 2, available at http://www.jcb.org/cgi/content/full/jcb.200801105/DC1; Heald et al., 1996). The average velocity of individual speckles was 2.75 ± 0.75 μm/min (mean ± SD; n = 34,713 trajectories from nine spindles; Fig. 2, B and C), similar to control spindles. The variation of the mean speckle velocities between spindles was again small (0.08 μm/min; n = 9 spindles) compared with flux variation within a spindle. Flux rates consistently decreased by ∼20% near spindle poles (Fig. 2, D–F). Previous FSM analyses had suggested that kinetochore microtubules flux slightly slower than nonkinetochore microtubules (Maddox et al., 2003a; Vallotton et al., 2003). Our results rule out the possibility that the slower rates near the poles and the variation between individual speckle velocities in control spindles are caused by different contributions of kinetochore versus nonkinetochore microtubules in different regions of the spindle.

Next, we tested the hypothesis that the flux velocity gradient could be associated with a regional variation of different classes of molecular motors inside the spindle. We perturbed the dynein/dynactin complex and kinesin-5, which are both essential for bipolar spindle assembly (Gaetz and Kapoor, 2004; Mitchison et al., 2005). Treatment of extract spindles with excess p50/dynamitin caused spindle pole defocusing (Fig. 3 A and Video 3, available at http://www.jcb.org/cgi/content/full/jcb.200801105/DC1; Wittman and Hyman, 1999). The mean flux velocity in these spindles was 2.14 ± 0.58 μm/min (mean ± SD; n = 23,768 trajectories from seven spindles; Fig. 3, B and C), only slightly slower than in control spindles. However, the regional flux variation was eliminated (Fig. 3, D–F), which is in agreement with the data in Burbank et al. (2007).

To test whether this effect was specific to the loss of dynein/dynactin function and focused poles, we inhibited the function of kinesin-5 using various doses of monastrol (Mayer et al., 1999). The mechanical support of glass slide and coverslip (see Image acquisition section) prevented the collapse of drug-treated spindles into monopoles (Miyamoto et al., 2004; Mitchison et al., 2005). At concentrations between 20 and 40 μM, the average flux rate decreased sharply by ∼55% to 1.16 ± 0.31 μm/min (n = 51,369 trajectories from 14 spindles; Fig. 3 G), in agreement with Miyamoto et al. (2004). However, in contrast to Miyamoto et al. (2004), our measurements suggested that between 50 and 150 μM, the flux rate stayed constant at 1.18 ± 0.32 μm/min (n = 60,875 trajectories from 20 spindles; Video 4, available at http://www.jcb.org/cgi/content/full/jcb.200801105/DC1). Above 150 μM, the flux rate decreased to 0.86 ± 0.29 μm/min (n = 13,364 trajectories from four spindles treated with monastrol at 200 μM).

Spatial analysis showed that monastrol treatment also eliminated the regional flux variation (Fig. 3, H–L; and Video 5, available at http://www.jcb.org/cgi/content/full/jcb.200801105/DC1). Between 20 and 200 μM, flux rates remained almost constant along the pole-to-pole axis (Fig. 3 M), indicating that under kinesin-5 inhibition, dynein/dynactin cannot generate the regional flux rate variation observed in control spindles. This contradicts the slide and cluster model (Burbank et al., 2007) that predicts decreased velocities at the poles as long as dynein/dynactin antagonizes poleward flux.

To further examine the requirement of dynein/dynactin and kinesin-5 functions for regional flux variation, we treated spindles with excess p50/dynamitin and 200 μM monastrol concurrently (Fig. 3 N and Video 6, available at http://www.jcb.org/cgi/content/full/jcb.200801105/DC1). This combination rescues focused pole spindle morphology (Miyamoto et al., 2004). The average flux rate in these spindles was 1.59 ± 0.39 μm/min (mean ± SD; n = 26,018 trajectories from six spindles; Fig. 3, N–P), lower than when only dynein/dynactin is inhibited. Loss of both dynein/dynactin and kinesin-5 function also eliminated the regional flux variation (Fig. 3, Q–S), indicating that a pole-based flux-driving mechanism

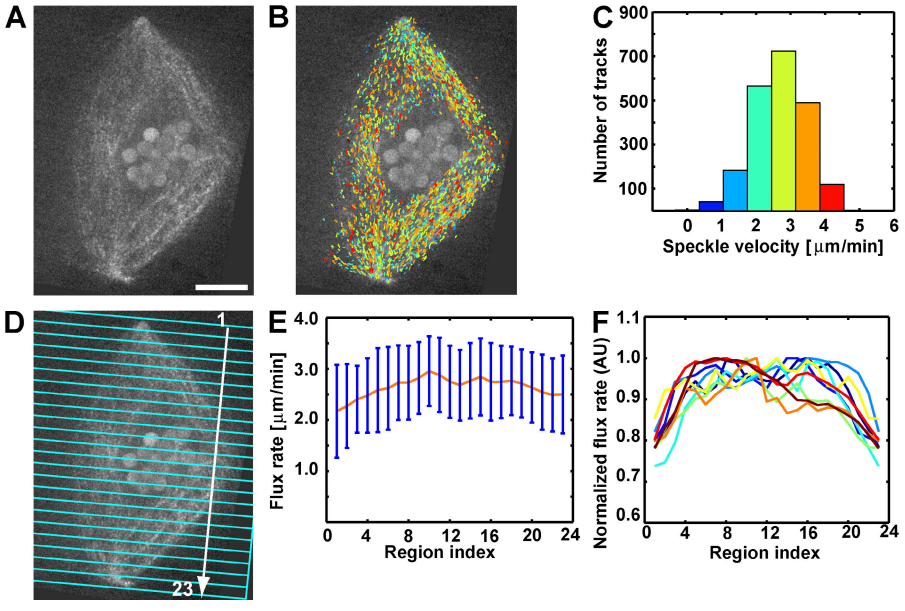

Figure 2. **Regional variation of poleward microtubule flux in spindles assembled around plasmid DNA-coated beads.** (A) X-rhodamine tubulin speckles and autofluorescent beads. (B and C) Speckle trajectories color coded according to the velocity histogram (C); the flux rate of the spindle shown is mean ± SD = 2.69 ± 0.74 μm/min (n = 2,128 trajectories). (D and E) Mean and SD (error bars) of speckle velocities within regions in D. (F) Spatial distributions of normalized microtubule velocities of nine bead spindles. Bar, 10 μm.

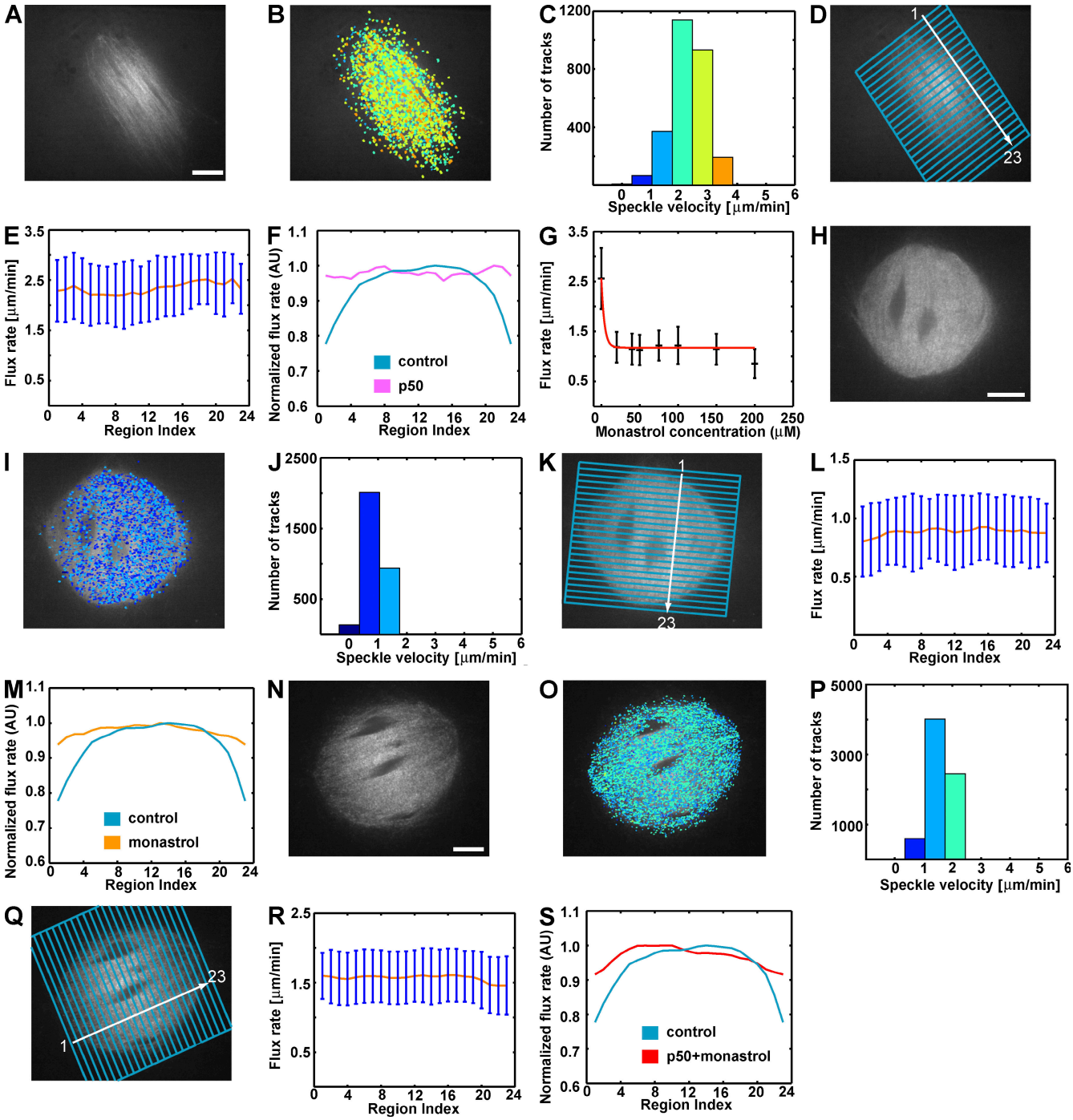

Figure 3. **Inhibition of dynein/dynactin, kinesin-5, or both suppresses regional variation of poleward microtubule flux.** (A) Spindle treated with excess p50/dynamitin. (B and C) Speckle trajectories color coded according to the velocity histogram (C); the flux rate of the specific spindle shown is mean ± SD = 2.33 ± 0.60 μm/min (n = 2,702 trajectories). (D and E) Mean and SD (error bars) of speckle velocities within regions in D. (F) Normalized flux rate along the pole-to-pole axis of control (average over 11 spindles) versus p50/dynamitin-treated spindles (average over seven spindles). (G) Flux rates at different monastrol concentrations. (H) Spindle treated with 200 μM monastrol. (I and J) Speckle trajectories color coded according to the velocity histogram (J); the flux rate of the spindle shown is mean ± SD = 0.89 ± 0.30 μm/min (n = 3,085 trajectories). (K and L) Mean and SD (error bars) of speckle velocities within regions in K. (M) Normalized flux rate distribution along the pole-to-pole axis of control and monastrol-treated spindles (average over 17 spindles treated with 20–200 μM monastrol). (N) Spindle treated with both 200 μM monastrol and excess p50/dynamitin. (O and P) Speckle trajectories color coded according to the velocity histogram (P); the flux rate of the spindle shown is mean ± SD = 1.59 ± 0.38 μm/min (n = 7,214 trajectories). (Q and R) Mean and SD (error bars) of speckle velocities within regions in Q. (S) Normalized flux rate distribution along the pole-to-pole axis of control versus monastrol + p50/dynamitin–treated spindles (average over six spindles). Bars, 10 μm.

independent of dynein/dynactin is not sufficient to generate regional flux variation.

Normality tests indicated that speckle velocities of control spindles did not follow a single normal distribution (Fig. 4 A). This raised the possibility that the velocity distribution originated from multiple modes, each one representing a distinct flux-driving mechanism. To test this, we applied statistical mode analysis (see Statistical analysis of speckle velocity distributions

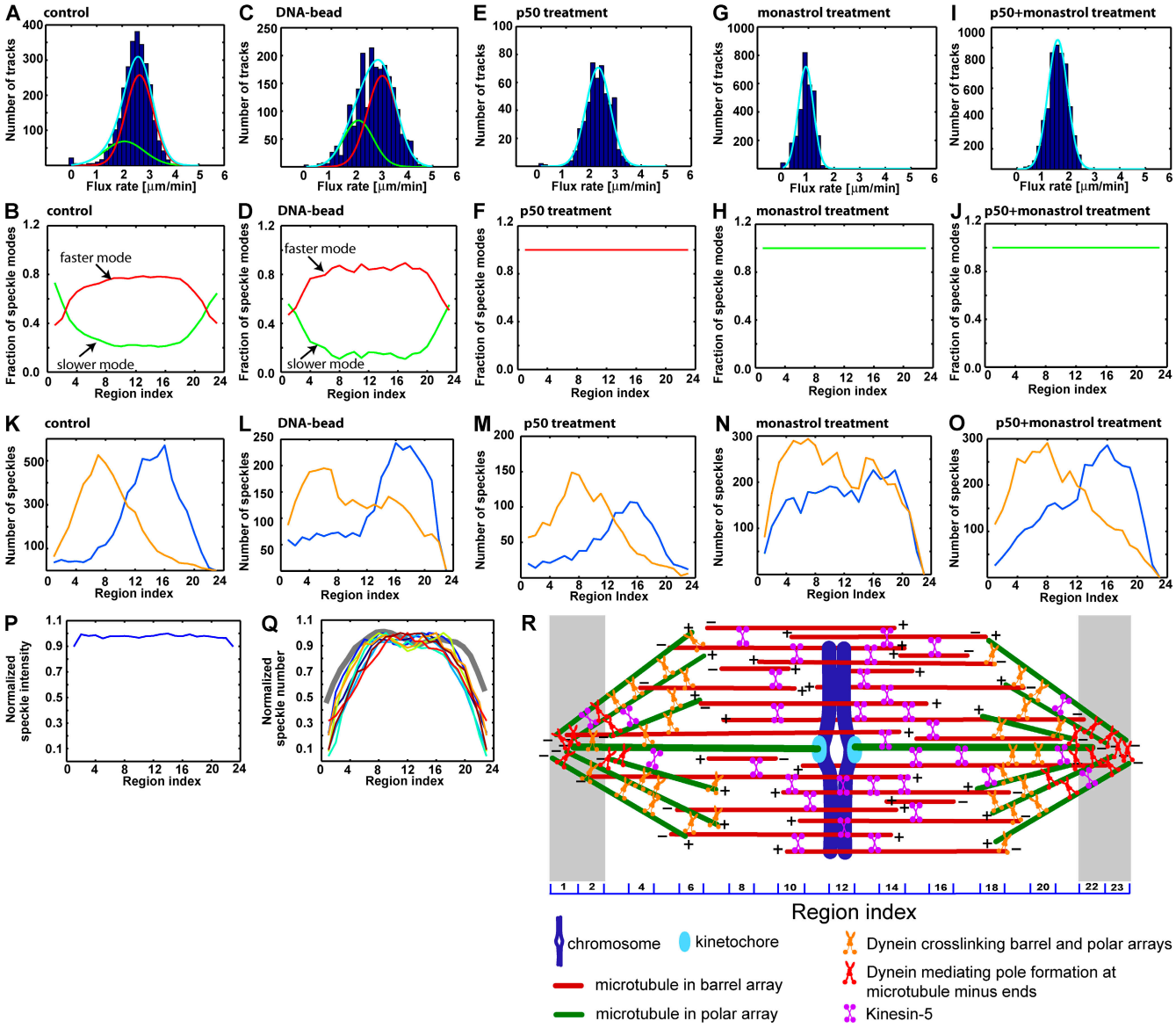

Figure 4. **Spatial organization of spindle microtubules.** (A, C, E, G, and I) Mode analysis of flux velocity distributions for representative individual spindles: the control spindle in Fig. 1 A (A), the DNA bead spindle in Fig. 2 A (C), the spindle treated with p50/dynamitin in Fig. 3 A (E), the spindle treated with 200 μM monastrol in Fig. 3 C (G), and the spindle treated with 200 μM monastrol and p50/dynamitin in Fig. 3 N (I). Red, fast mode; green, slow mode; cyan, mixture of both modes. (B, D, F, H, and J) Regional contribution of velocity modes. Averages of control spindles (B; $n = 11$), DNA bead spindles (D; $n = 9$), p50/dynamitin-treated spindles (F; $n = 7$), monastrol-treated spindles (H; $n = 7$), and monastrol and p50/dynamitin–treated spindles (J; $n = 6$). (K–O) Spatial distribution of speckle appearances of spindles analyzed in A, C, E, G, and I. Orange, speckles moving toward the left pole; blue, speckles moving toward the right pole. (P) Normalized distribution of average speckle intensity (average of 11 control spindles). (Q) Normalized speckle number along the pole-to-pole axis of nine control spindles. Gray, normalized speckle number of a spindle treated with 200 μM monastrol. (R) Model: two slow-fluxing polar microtubule arrays (green) are dynamically coupled via motors to a barrel array (red) with antiparallel microtubule polarity and faster flux velocities. Gray bands representing regions 1–2 and 22–23 define left and right poles in our analysis, respectively.

section; Schwarz, 1978; Fraley and Raftery, 2002) and found velocities to follow two and only two modes: 2.73 ± 0.48 versus 1.87 ± 0.53 μm/min (speckles pooled from 11 spindles). Accordingly, reduced flux rates at the poles could be related to the spatial shifting of two partially overlapping speckle populations, one moving at the faster velocity mode of ∼2.7 μm/min and the other at the slower velocity mode of ∼1.9 μm/min. To test this, we repeated the mode analysis separately for each of the 23 bands along the pole-to-pole axis. Speckle velocities in >90% of the regions follow two velocity modes. Then, we determined the fraction of speckles of each mode in each band (see Statistical analysis of speckle velocity distributions section; Fig. 4 B). The faster mode dominated near the midzone (∼80%:20%), and the slower mode dominated at the spindle poles (∼60%:40%).

In DNA bead spindles, speckle velocities also followed two modes (3.04 ± 0.60 μm/min vs. 1.95 ± 0.60 μm/min; pooled from $n = 9$ spindles; Fig. 4 C). As in control spindles, the midzone splits 80%:20% between fast and slow microtubule flux (Fig. 4 D). However, the 50%:50% split at the poles suggests that in these spindles, the faster fluxing microtubule population reaches further out into the polar regions.

Spindles in which dynein/dynactin, kinesin-5, or both were inhibited fluxed in a single velocity mode (Fig. 4, E, G, and I, examples under different conditions; Fig. 4 F, single mode at 2.20 ± 0.60 μm/min pooled from seven spindles treated with p50/dynamitin; Fig. 4 H, single mode at 1.15 ± 0.30 μm/min pooled from 17 spindles treated with monastrol; Fig. 4 J, single mode at 1.60 ± 0.40 μm/min pooled from six spindles treated with monastrol and p50/dynamitin). Although the mean values of the modes in these inhibited spindles do not quantitatively match the levels of the two modes in control or DNA bead spindles, we propose that dynein/dynactin inhibition eliminates a slower pole-based flux mechanism by causing spindle pole defocusing and that kinesin-5 inhibition eliminates fast antiparallel sliding of microtubules in the spindle midzone.

The single modes in spindles with disrupted motors were systematically slower than the corresponding modes in control spindles (1.2 and 1.6 μm/min vs. 1.9 μm/min for pole-driven flux; 2.2 vs. 2.7 μm/min for midzone-driven flux). We suggest these differences are caused by the effects of motor disruption on dynamic cross-links between differentially fluxing microtubules. Inhibition of dynein/dynactin may result in a more rigid binding of microtubules at the spindle pole with those in the midzone. This increases the mechanical resistance to kinesin-5–driven microtubule sliding and thus decreased flux rates in the midzone. Evidence for more rigid microtubule cross-linking under p50/dynamitin treatment also comes from single fluorophore speckle imaging showing reduced relative sliding of proximal individual microtubules (Yang et al., 2007). Inhibition of kinesin-5 also slows pole-based flux. Thus, flux perturbation in the spindle midzone causes immediate adjustment of flux rates at the poles. Concurrent inhibition of kinesin-5 and dynein/dynactin increases the pole-based flux relative to kinesin-5–inhibited spindles, suggesting that dynein/dynactin-mediated pole focusing in control and DNA spindles exerts mechanical resistance to pole-based flux. Together, these findings reveal the delicate balance of two flux-driving mechanisms contributing to the steady-state dynamics of metaphase spindles. In addition, they establish a dual role of dynein/dynactin in cross-linking microtubules. On one hand, dynein/dynactin mediates dynamic cross-links between differentially fluxing yet spatially overlapping microtubules of the spindle midzone and polar regions. On the other hand, by focusing microtubules into a pole, it enables the action of a pole-based flux mechanism but simultaneously generates mechanical resistance. We speculate that the change in dynein/dynactin function from a dynamic to a more static cross-linker is related to the motors reaching microtubule minus ends in the polar region.

To further understand how the spatial distribution of two velocity modes affects microtubule organization, we separated speckles based on flow direction and counted the number of speckle appearances within different regions along the pole-to-pole axis (Fig. 4, K–O). As in Burbank et al. (2006), we assumed that tubulin subunits are incorporated only at the microtubule plus ends and that labeled tubulins have equal probability to be incorporated into the microtubule network. Under these assumptions, and unless the speckle intensity exhibits systematic regional variation, the spatial density of microtubule plus ends is proportional to the density of speckle appearances, whereas the density of speckles fluxing through each spindle region is proportional to the density of microtubules. A systematic increase in speckle intensity within a certain region would suggest microtubule bundling. We did not find such variations in average speckle intensity (Fig. 4 P).

In control spindles, the highest number of microtubule plus ends was found halfway between the pole and the metaphase plate (Fig. 4 K). In contrast, the density of microtubules is constant throughout the midzone (Fig. 4 Q). Similar distributions of microtubule plus end density were detected in DNA bead spindles (Fig. 4 L), in dynein/dynactin-inhibited spindles (Fig. 4 M), and in spindles treated with low concentrations of monastrol (not depicted). However, in spindles treated with high concentrations of monastrol (∼200 μM), the two maxima were no longer well separated (Fig. 4 N). Concurrent dynein/dynactin and kinesin-5 inhibition rescued the microtubule plus end density distribution of control spindles (Fig. 4 O).

Together with the identification of two distinctly fluxing microtubule populations, these microtubule and plus end density distributions suggest a spindle architecture consisting of a barrel of microtubules in the spindle midzone with antiparallel polarity that connects two polar arrays of microtubules with uniform polarity (Fig. 4 R). Whereas short microtubules are found with equal probability in all three arrays (Yang et al., 2007), two observations provide evidence that long microtubules preferentially accumulate in the midzone barrel. First, the midzone contains a relatively low number of microtubule plus ends (Fig. 4 K) yet the highest number of microtubules (Fig. 4 Q). Therefore, a significant number of microtubules should have plus ends outside the midzone but span the entire barrel. Second, the majority of plus ends of microtubules that flux to the left pole are located in the left half of the spindle and vice versa for plus ends of microtubules that flux to the right pole (Figs. 1, B and C; and 4 K). However, ∼30% of spindle microtubules are longer than half the spindle length (see section Estimating the percentage of long microtubules…; Yang et al., 2007). To fit this population into the plus end distributions, the majority of microtubules with plus ends in the right half of the spindle and flux to the left must fully span the midzone and reach the left pole. The same holds true for microtubules with plus ends located in the left half spindle and flux to the right pole.

When dynein/dynactin was inhibited, the polar array became defocused but maintained its position relative to the barrel array (compare microtubule plus end distributions in Fig. 4, M and K). Inhibition of kinesin-5 increased microtubule overlap in the barrel array, as seen by the broader plus end distributions (Fig. 4 N). This caused a decreased barrel length. Indeed, the size of bipoles treated with 200 μM monastrol was ∼40% ($n = 6$) shorter than the size of control spindles ($n = 11$). As the distance between the two polar arrays becomes shorter, the region with a constant microtubule density is broadened (Fig. 4 Q, thick gray line). Concurrent dynein/dynactin and kinesin-5 inhibition restores the spatial separation of barrel and polar arrays (Fig. 4 O), and spindles are only slightly shorter (by ∼15%; $n = 6$) than control spindles ($n = 11$). However, more microtubules with flux to the left pole have plus ends in the right half-spindle and vice

versa for microtubules with flux to the right pole (Fig. 4 O). Thus, the average length of barrel microtubules must increase under dynein/dynactin inhibition, as shown in Yang et al. (2007).

In summary, our previous single fluorophore speckle analysis of *Xenopus* egg extract meiotic spindles established the tiled array of individually sliding short and long microtubules as a model for spindle construction. However, the low spatial density of single fluorophore speckles did not provide information on how the tiles are integrated globally. In this study, using the high density of multifluorophore speckles, we find that the spindle is composed of two polar arrays with short microtubules of uniform polarity and slow pole-driven flux and an interconnecting barrel array of long and short microtubules with antiparallel polarity and faster kinesin-5–driven flux. Interestingly, our barrel model is reminiscent of an early cartoon of spindle architecture in Alberts et al. (1983), which has been replaced in subsequent editions by a more pole-oriented model.

Materials and methods

Frog egg extracts and spindle assembly

Cytostatic factor–arrested *Xenopus* egg extracts were prepared as in Murray (1991) and Desai et al. (1999). To assemble spindles, extracts were cycled once through interphase and DNA replication and were held in mitosis by the addition of cytostatic factor–arrested extract. Spindle assembly around DNA-coated beads and assembly of plasmid DNA onto magnetic beads were performed as in Heald et al. (1996). All extract preparation and spindle assembly were performed at 18°C. Tubulin purified from porcine brain was labeled using X-rhodamine (Invitrogen) as in Hyman et al. (1991). In some experiments, AlexaFluor488-labeled anti-NuMA antibody (a gift from A. Groen, Harvard University, Cambridge, MA) was added to assembled structures to label spindle poles, mark the location of poles, verify bipolar and monopolar morphology, and facilitate identification of spindle structures in wide-field assays. Purified recombinant p50/dynamitin was prepared as in Wittman and Hyman (1999) and added at 0.9 mg/ml to the spindle assembly reaction after cycling the extract through interphase and DNA replication. Monastrol (Sigma-Aldrich) was added at various concentrations after bipolar spindle assembly. For coinhibition of dynein/dynactin and kinesin-5, purified recombinant p50/dynamitin was added at 0.9 mg/ml, whereas monastrol was added at 200 µM. Control and perturbed spindles were pressed between slide and coverslip in the same way and imaged under the same conditions.

Image acquisition

FSM was performed using both wide-field (Waterman-Storer et al., 1998) and spinning disk confocal fluorescence microscopy (Maddox et al., 2003b). Small aliquots (3.8 µl) of *Xenopus* egg extract containing spindles were placed on a glass slide and covered with an 18 × 18–mm coverslip and sealed with valap (1:1:1 vasoline, lanolin, and parafin). Imaging was performed at 21°C. Digital images were collected with a cooled CCD camera (Orca ER; Hamamatsu) mounted on a microscope (TE300; Nikon) with a 100×/1.4 NA plan Apochromat differential interference contrast objective (Nikon). MetaMorph software (MDS Analytical Technologies) was used to control shutters, wavelength selection, image acquisition, and storage. Images of fluorescently labeled tubulin were acquired at 3–10-s intervals depending on the experimental condition. In some experiments, paired AlexaFluor488 (AlexaFluor488-labeled anti-NuMA antibody) and -568 (X-rhodamine tubulin) images were collected sequentially within 1.5 s of each other to follow tubulin speckles and spindle poles.

FSM image analysis

Speckles were detected as in Ponti et al. (2003) and tracked as in Cameron et al. (2006). The velocity of a speckle, also referred to as the flux rate, was defined as the total distance it traveled along its trajectory divided by the trajectory lifetime.

The two halves of a spindle often have slightly different regional distributions of flux rates. This asymmetry was corrected for averaging and comparison of regional flux rate distributions from different spindles (Fig. 1 H) by equalizing average flux rates at the two poles (Fig. S1). Otherwise, the results would be strongly dependent on the arbitrarily selected directions of region index series in different spindles. First, a line (*AB*) is drawn between the two ends of the distribution curve. Then, for each region, the vertical distance (*d*) between its corresponding points on the flux rate distribution curve and *AB* is calculated. To calculate the corrected distribution curve, the average of flux rates at the two poles ($[V_1 + V_{23}]/2$) is used as the basis value. For each region, its corrected flux rate is then calculated as this basis value plus its distance, *d*, to *AB*. This procedure effectively rotates the original flux rate regional distribution curve so that the average flux rates at the two poles become equalized. Importantly, it preserves the relative distribution of mean flux rates along the pole-to-pole axis.

Relative rates of flux decrease in polar regions were calculated as $([V_{max} - V_1]/V_{max} + [V_{max} - V_{23}]/V_{max})/2$, where V_1 and V_{23} denote the mean flux rates within regions 1 and 23, respectively, and V_{max} is the maximum flux rate within the spindle. For most of the spindles, the maximum flux rate was observed near the middle of the spindle (Fig. 1 F).

Excluding spindle geometry as the source of flux reduction at the poles

The possibility that flux reduction at the poles would be mainly related to projection artifacts when imaging a three-dimensional scaffold of bended microtubules was excluded based on three sets of observations. (1) A projection effect would also cause a decrease in the SD of speckle velocities, which was not observed (Fig. 1 G). A more formal treatment of this argument is given in the section Decreases in the average velocity of speckles... (2) Spindles exhibited significant variation in morphologies but showed similar flux rate reduction near the poles (Fig. 1 H). (3) Switching from wide-field to spinning disk confocal microscopy yielded the same flux rate decrease near the poles despite the much narrower optical section (Fig. S2, available at http://www.jcb.org/cgi/content/full/jcb.200801105/DC1). Therefore, the flux rate reduction near poles is not a purely geometric effect but must be caused by spatially differential flux-driving mechanisms.

Statistical analysis of speckle velocity distributions

The normality of the distribution of speckle velocities under various experimental conditions was checked using multiple tests, including Lilliefors test, Anderson-Darling test, and Shapiro-Francia test, implemented in the Nortest package in *R*.

The modes of speckle velocity distribution were analyzed using the model-based clustering package MCLUST in *R* based on the technique described in Fraley and Raftery (2002). This method computes an optimal mixture (i.e., sum) of different normal distributions that best fits the given speckle velocity distribution. In this way, each speckle velocity mode is represented by a distinct normal distribution.

A critical property of this method is that it does not assume a priori the number of normal distribution modes. Instead, through optimization, it determines simultaneously the optimal number of modes and the optimal parameters for each mode (i.e., its mean and SD) by using the Bayesian information criterion (BIC; Schwarz, 1978), which is defined as $BIC \equiv 2\, log\, L_M(x, \hat{\theta}) - m_M\, log(n)$, where $log\, L_M(x, \hat{\theta})$ is the maximized logarithmic likelihood for the model, x is the random measurement variable, $\hat{\theta}$ is the optimal model parameter vector, m_M is the number of independent parameters (i.e., means and SDs of different modes) to be estimated, and n is the number of observations (sample size).

The first term of the BIC definition penalizes underfitting (i.e., poor fitting) of speckle velocity distributions with too few modes. The second term of the BIC definition penalizes overfitting of speckle velocity distributions with too many modes. In this way, BIC provides a balance between optimal fitting performance and model complexity. It allows the comparison of models with different parameters and different numbers of modes. Specifically, under the aforementioned definition, the best model is the one that gives the overall highest BIC. Because BIC depends on sample sizes, it is a relative criterion that can only be used to compare models for the same experiment.

In our analysis, we first checked the normality of speckle velocity distributions using several tests. The results for control spindles using the Anderson-Darling test are listed in Table S1 (available at http://www.jcb.org/cgi/content/full/jcb.200801105/DC1). The test consistently returned low p-values ($P < 0.001$) for all control spindles, indicating that speckle velocities in control spindles were not likely to follow a single normal distribution mode. Then, we used the aforementioned model-based clustering method and tested different models with mode numbers ranging from one to nine. In our analysis, models with one to three modes consistently ranked the highest and thus the best. For simplicity, we only listed in Table S1 the best BIC values under one, two, and three modes.

The BIC values are sorted for each control spindle. Models with the highest BIC are the most likely. With the exception of spindle 04, models with two modes give the highest (best) BIC. In comparison, models with three modes give lower (worse) BIC values, and models with one mode consistently give the lowest (worst) BIC values. Because BIC is defined on logarithmic scales, small differences between BIC values may still represent significant differences between models in terms of how well they fit the given speckle velocity distributions. In summary, Table S1 shows that two-mode models give the best fit of speckle velocity distributions in control spindles, whereas models with one or three modes are statistically significantly worse in terms of BIC.

Similar procedures were repeated for DNA bead spindles, monastrol-treated spindles, p50/dynamitin-treated spindles, and p50/dynamitin + monastrol–treated spindles. We have also checked this result by performing cluster analysis in the 23 individual regions of each spindle analyzed and counted the number of velocity modes. For control spindles, ~90% of the regions returned a two-mode distribution (23 regions for each spindle; $n = 11$ spindles). In comparison, >80% of the regions returned a single-mode distribution in p50/dynamitin-treated spindles (23 regions per spindle; $n = 7$), monastrol-treated spindles (23 regions per spindle; $n = 17$), and p50/dynamitin + monastrol–treated spindles (23 regions per spindle; $n = 6$).

After determining the modes over an entire spindle, the relative contribution of each of them to the speckle velocity distribution within region i ($i = 1…23$) was computed by fitting the cumulative speckle velocity distribution $P_i(v)$ with a mixture of cumulative distribution functions of normal distributed modes

$$D_k(v;\mu_k,\sigma_k) = \int_0^v \frac{1}{\sqrt{2\pi}\sigma_k} e^{-\frac{(v-\mu_k)^2}{2\sigma_k^2}} dv, k = 1..K,$$

where K denotes the total number of modes ($K = 2$ in control and DNA bead spindles) and v denotes speckle velocity. The mean and SD of each mode are denoted as μ_k and σ_k, respectively. The relative weight of each mode, c_k, was determined by minimizing the error function

$$e_i = \int_0^{v_{max}} \left(P_i(v) - \sum_{k=1}^{K} c_k D_k(v;\mu_k,\sigma_k) \right)^2 dv$$

using the nonlinear least-squares curve-fitting function *lsqnonlin* of MATLAB. Here, v_{max} represents the upper limit of speckle velocity and is determined by the search radius of speckle tracking and imaging condition. Because fitting is performed on the cumulative distribution, the constraint

$$\sum_{k=1}^{K} c_k = 1$$

is automatically satisfied.

Decreases in the average velocity of speckles as a result of bending of microtubules must be accompanied by similar decreases in the velocity SD

We represent the average velocity, V, of poleward-moving speckles within a selected region of the spindle as the weighted sum of the average velocity of N groups of speckles, each group following a different mode:

$$V = \sum_{i=1}^{N} c_i V_i,$$

where c_i and V_i denote the relative weight and the average velocity of each group (mode), respectively. Assuming that average velocities (V_i) of different groups (modes) are uncorrelated, the variance of V is determined by

$$\sigma^2(V) = \sum_{i=1}^{N} c_i^2 \sigma_i^2.$$

Under a potentially varying microtubule-bending angle of θ_i for each group, the SD of the projected (i.e., measured) average velocity of speckle movement in the camera image plane, denoted by σ_p, must become smaller because

$$\sigma_p^2(V) = \sum_{i=1}^{N} c_i^2 \times \cos^2\theta_i \times \sigma_i^2 < \sigma^2(V).$$

Furthermore, for each group, the mean and SD of speckle velocities have the same rate of decrease of $1 - \cos\theta_i$ under microtubule bending. Therefore, σ should decrease at a rate similar to that of V. However, no decrease in σ was observed in our data (Fig. 1 G).

Estimating the percentage of long microtubules from the truncated normal distribution of spindle microtubule length

The truncated normal distribution of control spindle microtubule length in Yang et al. (2007) was normalized with respect to the mean spindle length. The mean and SD of the normalized truncated normal distribution were calculated to be 0.41 and 0.25, respectively. From this normalized distribution, the percentage of microtubules whose length is >0.5 (i.e., half the spindle length) was determined to be ~30%.

Online supplemental material

Fig. S1 shows additional results on detection and tracking of speckles, flux rate variation analysis, and a color-coded map of the complete spatial distribution of microtubule flux rate within a control spindle. Fig. S2 shows the analysis of flux rate distribution in a control spindle imaged using spinning disk confocal microscopy. Table S1 lists BIC values used to determine numbers of speckle velocity modes in control spindles. Video 1 corresponds to Fig. 1 A and shows tracking of individual speckles in antiparallel movement. Video 2 corresponds to Fig. 2 A and shows flux in a spindle assembled around DNA-coated beads. Video 3 corresponds to Fig. 3 A and shows flux in a spindle treated with excess p50/dynamitin. Video 4 shows flux in a spindle treated with 100 µM monastrol. Video 5 corresponds to Fig. 3 H and shows flux in a spindle treated with 200 µM monastrol. Video 6 corresponds to Fig. 3 N and shows flux in a spindle treated with excess p50/dynamitin and 200 µM monastrol. Online supplemental material is available at http://www.jcb.org/cgi/content/full/jcb.200801105/DC1.

We thank Ben Moree for assistance with image collection and Tom Maresca and Jay Gatlin for comments on the manuscript.

This work was supported by National Institutes of Health grants GM60678 to E.D. Salmon and G. Danuser and GM24364 to E.D. Salmon.

Submitted: 22 January 2008
Accepted: 23 July 2008

References

Alberts, B., D. Bray, J. Lewis, M. Raff, K. Roberts, and J.D. Watson. 1983. Molecular Biology of the Cell. Garland Publishing, New York. 1146 pp.

Burbank, K.S., A.C. Groen, Z.E. Perlman, D.D. Fisher, and T.J. Mitchison. 2006. A new method reveals microtubule minus ends throughout the meiotic spindle. *J. Cell Biol.* 175:369–375.

Burbank, K.S., T.J. Mitchison, and D.S. Fisher. 2007. Slide-and-cluster models for spindle assembly. *Curr. Biol.* 17:1373–1383.

Buster, D.W., D. Zhang, and D.J. Sharp. 2007. Poleward tubulin flux in spindles: regulation and function in mitotic cells. *Mol. Biol. Cell.* 18:3094–3104.

Cameron, L.A., G. Yang, D. Cimini, J.C. Canman, O.K. Evgenieva, A. Khodjakov, G. Danuser, and E.D. Salmon. 2006. Kinesin 5-independent poleward flux of kinetochore microtubules in PtK1 cells. *J. Cell Biol.* 173:173–179.

Desai, A., A. Murray, T.J. Mitchison, and C. Walczak. 1999. The use of *Xenopus* egg extracts to study mitotic spindle assembly and function in vitro. *Methods Cell Biol.* 61:385–412.

Fraley, C., and A.E. Raftery. 2002. Model-based clustering, discriminant analysis, and density estimation. *J. Am. Stat. Assoc.* 97:611–631.

Gaetz, J., and T.M. Kapoor. 2004. Dynein/dynactin regulates metaphase spindle length by targeting depolymerizing activities to spindle poles. *J. Cell Biol.* 166:465–471.

Ganem, N.J., and D.A. Compton. 2004. The KinI kinesin Kif2a is required for bipolar spindle assembly through a functional relationship with MCAK. *J. Cell Biol.* 166:473–478.

Ganem, N.J., K. Upton, and D.A. Compton. 2005. Efficient mitosis in human cells lacking poleward microtubule flux. *Curr. Biol.* 15:1827–1832.

Heald, R., R. Tournebize, T. Blank, R. Sandaltzopoulos, P. Becker, A. Hyman, and E. Karsenti. 1996. Self-organization of microtubules into bipolar spindles around artificial chromosomes in *Xenopus* egg extracts. *Nature.* 382:420–425.

Hyman, A., D. Drechsel, D. Kellogg, S. Salser, K. Sawin, P. Steffen, L. Wordeman, and T. Mitchison. 1991. Preparation of modified tubulins. *Methods Enzymol.* 196:478–485.

Kapitein, L.C., E.J.G. Peterman, B.H. Kwok, J.H. Kim, T.M. Kapoor, and C.F. Schmidt. 2005. The bipolar mitotic kinesin Eg5 moves on both microtubules that it crosslinks. *Nature.* 435:114–118.

Kwok, B.H., and T.M. Kapoor. 2007. Microtubule flux: drivers wanted. *Curr. Opin. Cell Biol.* 19:36–42.

Maddox, P., A. Straight, P. Coughlin, T.J. Mitchison, and E.D. Salmon. 2003a. Direct observation of microtubule dynamics at kinetochores in *Xenopus* extract spindles: implications for spindle mechanics. *J. Cell Biol.* 162:377–382.

Maddox, P.S., B. Moree, J.C. Canman, and E.D. Salmon. 2003b. A spinning disk confocal microscope system for rapid high resolution, multimode, fluorescent speckle microscopy and GFP imaging in living cells. *Methods Enzymol.* 360:597–617.

Maiato, H., A. Khodjakov, and C.L. Rieder. 2005. *Drosophila* CLASP is required for the incorporation of microtubule subunits into fluxing kinetochore fibres. *Nat. Cell Biol.* 7:42–47.

Mayer, T.U., T.M. Kapoor, S.J. Haggarty, R.W. King, S.L. Schreiber, and T.J. Mitchison. 1999. Small molecule inhibitor of mitotic spindle bipolarity identified in a phenotype-based screen. *Science.* 286:971–974.

Mitchison, T.J. 1989. Polewards microtubule flux in the mitotic spindle - evidence from photoactivation of fluorescence. *J. Cell Biol.* 109:637–652.

Mitchison, T.J. 2005. Mechanism and function of poleward flux in *Xenopus* extract meiotic spindles. *Philos. Trans. R. Soc. Lond. B. Biol. Sci.* 360:623–629.

Mitchison, T.J., P. Maddox, J. Gaetz, A. Groen, M. Shirasu, A. Desai, E.D. Salmon, and T.M. Kapoor. 2005. Roles of polymerization dynamics, opposed motors, and a tensile element in governing the length of *Xenopus* extract meiotic spindles. *Mol. Biol. Cell.* 16:3064–3076.

Miyamoto, D.T., Z.E. Perlman, K.S. Burbank, A.C. Groen, and T.J. Mitchison. 2004. The kinesin Eg5 drives poleward microtubule flux in *Xenopus laevis* egg extract spindles. *J. Cell Biol.* 167:813–818.

Murray, A.W. 1991. Cell cycle extracts. *Methods Cell Biol.* 36:581–605.

Ohi, R., K. Burbank, Q. Liu, and T.J. Mitchison. 2007. Nonredundant functions of kinesin-13s during meiotic spindle assembly. *Curr. Biol.* 17:953–959.

Ponti, A., P. Vallotton, W.C. Salmon, C.M. Waterman-Storer, and G. Danuser. 2003. Computational analysis of F-actin turnover in cortical actin meshworks using fluorescent speckle microscopy. *Biophys. J.* 84:3336–3352.

Rogers, G.C., S.L. Rogers, T.A. Schwimmer, S.C. Ems-McClung, C. Walczak, R.D. Vale, J.M. Scholey, and D.J. Sharp. 2004. Two mitotic kinesins cooperate to drive sister chromatid separation during anaphase. *Nature.* 427:364–370.

Rogers, G.C., S.L. Rogers, and D.J. Sharp. 2005. Spindle microtubules in flux. *J. Cell Sci.* 118:1105–1116.

Schwarz, G. 1978. Estimating the dimension of a model. *Ann. Statist.* 6:461–464.

Shirasu-Hiza, M., Z.E. Perlman, T. Wittmann, E. Karsenti, and T.J. Mitchison. 2004. Eg5 causes elongation of meiotic spindles when flux-associated microtubule depolymerization is blocked. *Curr. Biol.* 14:1941–1945.

Vallotton, P., A. Ponti, C.M. Waterman-Storer, E.D. Salmon, and G. Danuser. 2003. Recovery, visualization, and analysis of actin and tubulin polymer flow in live cells: a fluorescence speckle microscopy study. *Biophys. J.* 85:1289–1306.

Waterman-Storer, C.M., A. Desai, J.C. Bulinski, and E.D. Salmon. 1998. Fluorescent speckle microscopy, a method to visualize the dynamics of protein assemblies in living cells. *Curr. Biol.* 8:1227–1230.

Wittman, T., and A. Hyman. 1999. A recombinant p50/dynamitin as a tool to examine the role of dynactin in intracellular processes. *In* Methods of Cell Biology. Vol 61. Academic Press, San Diego. 137–143.

Yang, G., A. Matov, and G. Danuser. 2005. Reliable tracking of large-scale dense antiparallel particle motion for fluorescent live cell imaging. *Proc. IEEE Int. Conf. Computer Vision and Pattern Recognition*. 3:138.

Yang, G., B.H. Houghtaling, J. Gaetz, J.Z. Liu, G. Danuser, and T.M. Kapoor. 2007. Architectural dynamics of the meiotic spindle revealed by single-fluorophore imaging. *Nat. Cell Biol.* 9:1233–1242.

Zhang, D., G.C. Rogers, D.W. Buster, and D.J. Sharp. 2007. Three microtubule severing enzymes contribute to the "Pacman-flux" machinery that moves chromosomes. *J. Cell Biol.* 177:231–242.